Diffusion model for ultrasound-modulated light

Joseph L. Hollmann
Roarke Horstmeyer
Changhuei Yang
Charles A. DiMarzio

Diffusion model for ultrasound-modulated light

Joseph L. Hollmann,[a,b,][*] **Roarke Horstmeyer,**[c] **Changhuei Yang,**[c] **and Charles A. DiMarzio**[a,b,d]
[a]Northeastern University, Department of Electrical and Computer Engineering, 409 Dana Research Center, 360 Huntington Avenue, Boston, Massachusetts 02115
[b]Gordon Center for Subsurface Sensing and Imaging Systems (CenSSIS), 360 Huntington Avenue, 302 Stearns Center, Boston, Massachusetts 02115
[c]California Institute of Technology, Department of Electrical Engineering, 1200 E. California Blvd. Mail Code 136-93, Pasadena, California 91125
[d]Northeastern University, Department of Mechanical and Industrial Engineering, 334 Snell Engineering Center, 360 Huntington Avenue, Boston, Massachusetts 02115

Abstract. Researchers use ultrasound (US) to modulate diffusive light in a highly scattering medium like tissue. This paper analyzes the US–optical interaction in the scattering medium and derives an expression for the US-modulated optical radiance. The diffusion approximation to the radiative transport equation is employed to develop a Green's function for US-modulated light. The predicted modulated fluence and flux are verified using finite-difference time-domain simulations. The Green's function is then utilized to illustrate the modulated reflectance as the US–optical interaction increases in depth. The intent of this paper is to focus on high US frequencies necessary for high-resolution imaging because they are of interest for applications such as phase conjugation. © 2014 Society of Photo-Optical Instrumentation Engineers (SPIE) [DOI: 10.1117/1.JBO.19.3.035005]

Keywords: ultrasound modulation of light; diffusion; finite-difference time-domain.

Paper 130709RR received Sep. 29, 2013; revised manuscript received Jan. 29, 2014; accepted for publication Jan. 30, 2014; published online Mar. 17, 2014.

1 Introduction

Precise measurements of physiological parameters are necessary to increase the accuracy of medical diagnostics, thus reducing unwanted surgical procedures, such as biopsies. Optical methods are well suited for this task, but their resolution degrades quickly with imaging depth because biological tissue is typically highly scattering. For example, confocal microscopy offers a resolution of 1 to 2 μm but is limited to an imaging depth of 100 to 300 μm.[1] Optical coherence tomography is able to increase the imaging depth at the cost of resolution.

However, several techniques combining ultrasound (US) and optical measurements have been developed to increase resolution and imaging depth while maintaining biological sensitivity. One such method mixes a focused US beam with light in tissue to create a diffusive wave modulated at the US frequency, which may then be measured utilizing interferometry, or a system capable of collecting an image at the US frequency.[2–4] Kothapalli et al.[5] utilized this method with US frequencies up to 75 MHz to experimentally obtain image resolutions in the tens of microns.

Recently, it has been shown that the US-modulated light can be used as a guidestar, and the frequency-shifted wavefront can be utilized to correct for the effects of scattering.[6,7] This technique can achieve US-resolution images at depths of several millimeters.[7] It has recently been shown that this method can achieve lateral resolutions of 5 μm by the use of initial probe beam wavefront permutation and optimization.[8]

The interaction of light and sound in an optically clear medium has been understood for over 80 years.[9] However, the interaction is much harder to predict in a scattering medium, such as biological tissue. A model was put forth for US modulation of an optical signal in an infinite homogeneous scattering medium[10] and solved using a Monte Carlo simulation.[11] This model was later improved upon for a US plane wave in an arbitrary medium.[12–16] Other work has ignored the coherent effects of light scattering and treats diffuse light using the radiative transport equation (RTE).[17] Recently, Hollmann et al.[18] developed a finite-difference time-domain (FDTD) model that is capable of solving for the modulated field. These simulations all have the disadvantage of being computationally intensive and requiring long run times, although efforts have been made in parallelizing and executing the Monte Carlo code on relatively quick graphical processing units.[19,20]

This paper will relate the incident optical flux and fluence rate, and the depth and strength of the US beam, to the resulting diffuse optical signal. We will accomplish this by linking the initial and US-modulated optical field, and develop a relationship for the US-modulated radiance. We will use this to develop a Green's function for the modulated diffusive wave.

The intent of this paper is to focus on high US frequencies necessary for high-resolution imaging because they are of interest for applications such as phase conjugation. This paper will focus on experimental systems that use frequencies of 45 MHz and above to achieve high-resolution images.[7,8] The results will be validated using an FDTD simulation developed previously.[18] After validating the model, we will use the results to develop a closed-form diffusion equation for the modulated sidebands.

2 Diffusion

We will review photon transport through a scattering medium and the diffusion approximation to the RTE[21] in this section. Several authors offer a thorough discussion on this subject.[22–24] However, we will briefly review the salient features here. The fluence rate describes the energy flow per unit area per unit time and is independent of flow direction:

*Address all correspondence to: Joseph L. Hollmann, E-mail: joe1h@aol.com

$$\Phi(\vec{r}, t) = \iint L(\vec{r}, \hat{\Omega}, t) \mathrm{d}^2\hat{\Omega} \tag{1}$$

where L is the radiance at position $\vec{r}$, traveling in the direction $\hat{\Omega}$ at time t. An infinitesimally small solid angle is described by $d^2\hat{\Omega}$. The flux describes the net energy flow per unit area per unit time:

$$\vec{J}(\vec{r}, t) = \iint L_r(\vec{r}, \hat{\Omega}, t) \cdot \hat{\Omega} \mathrm{d}^2\hat{\Omega} \tag{2}$$

The quantities L, Φ, and $\vec{J}$ have units of power per area and are fundamentally incoherent. A homogeneous turbid medium is modeled as having a scattering coefficient (μ_s) that quantifies the scatterer's cross-sectional area per unit volume. The medium also has an absorption coefficient (μ_a), which similarly describes the absorber's cross-sectional area per unit volume. The scattering anisotropy (g) is the average cosine of the scattered field resulting from a plane wave interacting with a single scatterer. However, the diffusion equation requires scattering to be isotropic, so an equivalent reduced, or transport, scattering coefficient is given by $\mu_s' = \mu_s(1 - g)$. A transport mean-free path describes the length after which a light ray loses memory of its incoming direction and is given as $\ell_t' = (\mu_s' + \mu_a)^{-1}$.

The radiance and source term may be expanded using spherical harmonics. Truncating the expansion after the second-term results in the P_1 approximation to the RTE, or

$$L(\vec{r}, \hat{\Omega}, t) = \frac{1}{4\pi}\Phi(\vec{r}, t) + \frac{3}{4\pi}\vec{J}(\vec{r}, t) \cdot \hat{\Omega}. \tag{3}$$

Solving the RTE with this approximation in a turbid medium leads to the diffusion equation

$$-D\nabla^2\Phi(\vec{r}, t) + c\mu_a\Phi(\vec{r}, t) + \frac{\delta\Phi(\vec{r}, t)}{\delta t}$$
$$+ \frac{3D}{c}\left[\mu_a\frac{\delta\Phi(\vec{r}, t)}{\delta t} + \frac{1}{c}\frac{\delta^2\Phi(\vec{r}, t)}{\delta t^2}\right]$$
$$= cQ_0(\vec{r}, t) - 3D\nabla \cdot \vec{Q}_1(\vec{r}, t) + \underline{\frac{3D}{c}\frac{\delta Q_0(\vec{r}, t)}{\delta t}}, \tag{4}$$

where $D = c/3(\mu_a + \mu_s')$ is the diffusion coefficient, and $Q_0(\vec{r}, t)$ and $\vec{Q}_1(\vec{r}, t)$ are monopole and dipole source terms, respectively.[22] Typically, Eq. (4) is simplified by assuming the scattering frequency is much larger than the modulation frequency and neglecting the underlined terms.[22,23]

The source term from the RTE is expanded in a similar manner and results in a monopole and dipole term. The monopole is given as

$$Q_0(\vec{r}, t) = \nabla \cdot \vec{J}(\vec{r}, t) + \mu_a\Phi(\vec{r}, t) + \underline{\frac{1}{c}\frac{\delta}{\delta t}\Phi(\vec{r}, t)}, \tag{5}$$

and the dipole is

$$\vec{Q}_1(\vec{r}, t) = \frac{1}{3}\nabla\Phi(\vec{r}, t) + \mu_t'\vec{J}(\vec{r}, t) + \underline{\frac{1}{c}\frac{\delta}{\delta t}\vec{J}(\vec{r}, t)}. \tag{6}$$

The underlined terms may be ignored.[22] Using this simplification, the fluence rate may be written in terms of a differential equation:

$$\left(\nabla^2 - \frac{\mu_a}{D} - \frac{1}{D}\frac{\delta}{\delta t}\right)\Phi(\vec{r}, t) = -3\mu_t'Q_0(\vec{r}, t) + 3\nabla \cdot \vec{Q}_1(\vec{r}, t). \tag{7}$$

Another simplification occurs by assuming the scalar and vector sources are viewed at a large enough distance that they appear to be a single isotropic point source. The new point source is, therefore, given an offset in the direction of the flux.[22,25] The approximations utilized to derive the diffusion equation limit its region of validity to distances greater than one ℓ_t' away from the source.

Typical applications utilizing the diffusion equation include a boundary between the turbid medium and a nonscattering medium, such as air or water. This interface is normally accounted for by using the extrapolated boundary conditions, which stipulate there is an equal but opposite point source located on the opposite side of the boundary that forces the fluence rate to be zero at some distance above the interface.[23] Furthermore, the extrapolated boundary conditions utilize scale factors for the fluence rate and flux to account for any index of refraction mismatch. Solving for these scale factors can be complicated, but tables and linear models of these coefficients exist elsewhere.[26,27]

3 US Modulation

This section will relate the field of the probe beam to the radiance of the US-modulated diffusive wave. The modulated field will then be related to the fluence and flux of the diffusive wave. We will then use this relationship to create the monopole and dipole sources discussed in the previous section.

A focused US beam with an angular frequency, ω_{us}, will interact with the optical signal by linearly modulating the local index of refraction and introduce a phase delay in the probe field. Although there is a potential for other US–optical interactions through the displacement or deformation of scattering particles, these effects are assumed to be minimal at high frequencies. This is because it has been shown that the importance of the index of refraction modulation grows exponentially larger than particle displacement with decreasing US wavelength.[10] Likewise, nonlinear effects, such as particle motion due to radiation pressure and heating, may also exist, but these effects do not produce modulation at the US frequency. This US model is similar to previously published US–optical simulations.[18]

3.1 Modeling US Modulation

In this section, we will model the US interaction with the optical probe field. A monochromatic optical field may be described as

$$E = Ae^{jw_o t}, \tag{8}$$

where $\omega_o = 2\pi f_o$ is the wavenumber, and f_o is the optical frequency of the light. As the field travels through the medium, it experiences a phase delay given by

$$\phi = k \times \mathrm{OPL}, \tag{9}$$

where $k = 2\pi/\lambda$ is the magnitude of the wave vector ($\vec{k}$) in a vacuum and the optical path length is

$$\mathrm{OPL} = \int_\alpha^\beta n(s)\mathrm{d}s, \tag{10}$$

where the integral is over the path taken from point α to β, and $n(s)$ is the index of refraction at position s. We can coherently sum the total field contribution at a given position

$$E_T = \sum_g^G A_g e^{j(w_o t + \phi_g)}, \tag{11}$$

where G is the total number of discrete wave fronts arriving at the given position. Similarly, the average net energy flow, or Poynting vector, is given as

$$\vec{S} = \frac{1}{\eta} \sum_g^G A_g A_g^* \frac{\vec{k}_g}{k}, \tag{12}$$

where and and μ_0 are the electromagnetic permittivity and permeability of free space, respectively. The direction of travel is given by $\vec{k}/k$.

Assuming a linear relationship between pressure and index of refraction, the time-varying optical phase delay induced by the US beam is

$$\phi_{\mathrm{us}} = M e^{j\omega_{\mathrm{us}} t} + M^* e^{-j\omega_{\mathrm{us}} t}, \tag{13}$$

where M describes the US modulation and ω_{us} is the US angular frequency. $|M|$ is the maximum phase change induced in the field and ΔM is the phase delay relative to the electronic oscillator driving the US transducer. As mentioned above, the phase change due to the US beam is small, so the field may be expanded using a first-order Maclaurin series or

$$E = A e^{j(\omega_o t + \phi_{\mathrm{us}})}$$
$$\approx A e^{j\omega_o t}(1 + jM e^{j\omega_{\mathrm{us}} t} + jM^* e^{-j\omega_{\mathrm{us}} t}). \tag{14}$$

The result is that the small phase modulation produces two sidebands at the frequencies $f_o \pm f_{\mathrm{us}}$.

3.2 Field-Radiance Relationship

This section reviews the relationship between the field and the radiance. This will allow us to use the results in Sec. 3.1 to relate the probe beam field to the radiance modulated at f_{us}. To accomplish this, we first decompose the electric field in an infinitesimally small area into a series of angle-dependent plane waves, as shown in Fig. 1. Each angular-dependent plane wave has the form

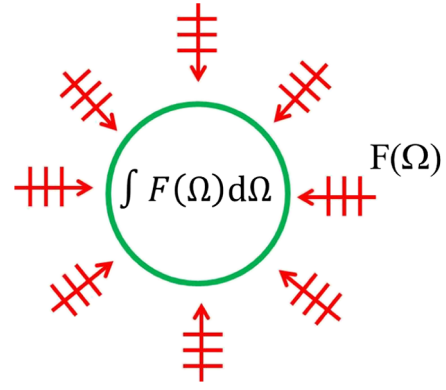$$F(\hat{\Omega}) = A(\hat{\Omega}) e^{j\omega_o t}, \tag{15}$$

where $A(\hat{\Omega})$ is the complex amplitude of the field. The field is described by the coherent combination of F over all $\hat{\Omega}$.

$$E = \iint F(\hat{\Omega}) \mathrm{d}^2 \hat{\Omega}. \tag{16}$$

In a scattering medium, $F(\hat{\Omega})$ is uncorrelated so that

$$\langle F(\hat{\Omega}) F^*(\hat{\Omega}') \rangle = 0, \tag{17}$$

for $\hat{\Omega} \neq \hat{\Omega}'$. The brackets, $\langle \rangle$, refer to the expected value of the field term. In Monte Carlo the expectation operation is handled by randomly varying the scatterers in the medium during the

Fig. 1 The field in an infinitesimally small volume is decomposed into a series of angle-dependent plane waves, $F(\hat{\Omega})$.

simulation.[28] The decomposition of the electric field may be related to the incoherent irradiance:

$$I = \left\langle \frac{1}{\eta} E E^* \right\rangle = \left\langle \frac{1}{\eta} \iint F(\hat{\Omega}) \mathrm{d}^2 \hat{\Omega} \iint F^*(\hat{\Omega}') \mathrm{d}^2 \hat{\Omega}' \right\rangle$$
$$= \left\langle \iiiint \frac{1}{\eta} F(\hat{\Omega}) F^*(\hat{\Omega}') \delta(\hat{\Omega} - \hat{\Omega}') \mathrm{d}\hat{\Omega} \mathrm{d}\hat{\Omega}' \right\rangle, \tag{18}$$

where the Dirac delta function is a result of Eq. (17). The wave impedance of the medium is given by $\eta = \sqrt{\mu_0/\varepsilon}$.

$$I = \frac{1}{\eta} \left\langle \iint F(\hat{\Omega}) F^*(\hat{\Omega}) \mathrm{d}^2 \hat{\Omega} \right\rangle. \tag{19}$$

The incoherent irradiance is related to the radiance[29] by

$$L \mathrm{d}^2 \hat{\Omega} = dI. \tag{20}$$

We use this relationship and the definition in Eq. (1) to write the fluence rate in terms of the field:

$$\Phi = \left\langle \frac{|E|^2}{\eta} \right\rangle. \tag{21}$$

Similarly, the flux describes the current density and may be written as

$$J = \langle \vec{S} \rangle, \tag{22}$$

where $\vec{S}$ is the Poynting vector and is the result of the cross product

$$\vec{S} = \frac{1}{2} (\vec{E} \times \vec{H}^*), \tag{23}$$

and $\vec{H}^*$ is the complex conjugate of the magnetic field.

3.3 US Modulated Radiance

We will use the relationship between the radiance and the field shown above to find the radiance modulated at the US frequency in terms of the optical probe field. We will then employ the discussion in Sec. 2 to find the US-modulated fluence rate and flux.

The US beam creates a positive and negative sideband and the resulting field is described by Eq. (14). To simplify notation,

the unmodulated field will be denoted with a subscript 0, and the modulated negative and positive sidebands will be described by subscripts $-$ and $+$, respectively. We will now rewrite the total field as

$$E_{\mathrm{us}} = E_0 + E_- + E_+. \tag{24}$$

Similarly, the US-modulated radiance in an infinitesimally small solid angle may be found by using Eqs. (19) and (20):

$$L_{\mathrm{us}} d^2\hat{\Omega} = d\Phi_{\mathrm{us}} = \left\langle \frac{|F_0 + F_- + F_+|^2}{\eta} \right\rangle d^2\hat{\Omega}, \tag{25}$$

where F_0, F_+, and F_- are the angular expansions of the field for the baseband, and upper and lower frequency components, respectively. Expanding the terms in a manner similar to Eq. (14) yields

$$L_{\mathrm{mod}} d^2\hat{\Omega} = \left\langle \frac{|A|^2}{\eta}(1 + 2|M|^2 + jMe^{j\omega_{\mathrm{us}}t} - jM^*e^{j\omega_{\mathrm{us}}t} \right.$$
$$\left. + jM^*e^{-j\omega_{\mathrm{us}}t} - jMe^{-j\omega_{\mathrm{us}}t} + |M|^2 e^{j2\omega_{\mathrm{us}}t} + |M|^2 e^{-j2\omega_{\mathrm{us}}t}) \right\rangle. \tag{26}$$

The reader is reminded that M is a complex quantity containing the phase modulation. The resulting modulated radiance has dc, and $\pm f_{\mathrm{us}}$ and $\pm 2f_{\mathrm{us}}$ terms. Typically, the amount of power modulated into the second order is negligible, so we will drop it from our discussion here. The ac radiance contains the components

$$L(\pm f_{\mathrm{us}}) d^2\hat{\Omega} = j\left\langle \frac{1}{\eta}|A(\hat{\Omega})|^2((M - M^*)e^{j\omega_{\mathrm{us}}t} \right.$$
$$\left. - (M^* - M)e^{-j\omega_{\mathrm{us}}t}) \right\rangle. \tag{27}$$

As described in Sec. 3.1, the US modulation in an infinitesimally small area introduces a small phase delay and is purely imaginary. As a result, the positive and negative modulated diffusive waves must be treated separately (as in Sec. 3.3) at the point of modulation or the modulated radiance will appear to be zero. It is important to note that as the fields propagate, the coherent addition described in Eq. (11) changes. As a result, they are no longer purely imaginary and we will see amplitude modulation. Focusing on the radiance modulated into the positive frequencies, we get

$$L(f_{\mathrm{us}}) d^2\hat{\Omega} = 2\left\langle \frac{|A|^2}{\eta} M e^{j\omega_{\mathrm{us}}t} \right\rangle. \tag{28}$$

Building upon this result and employing Eqs. (19) and (21) allows the modulated fluence rate at the US beam to be written as

$$\Phi_{ac} = j2\Phi_0 \Delta n k\ell, \tag{29}$$

where the subscript ac will imply the signal is modulated at the US frequency for the rest of this paper. The reader is reminded the modulation is due to a US-induced phase delay as described in Eq. (13). Similarly, the modulated flux is

$$\vec{J}_{ac} = j2\vec{J}_0 \Delta n k\ell. \tag{30}$$

It is important to remember that the j represents a 90-deg phase shift from the probe beam.

In this section, we have related the modulated radiance to the probe radiance. We have used this relationship to define the modulated fluence rate and flux in terms of the probe beam's fluence and flux. It is important to note this analysis assumes the US acts to create a small index of refraction change. We are assuming the frequency is high enough so that particle motion may be neglected.

4 Equivalent Sources

In this section, we will develop equations for the monopole and dipole sources in Eq. (3). We will then create a single effective source for our Green's function that accounts for the effects of both sources.

The diffusion equation for the modulated radiance may be written in terms of the modulated fluence and flux:

$$L_{ac} = \frac{j}{4\pi}\Phi_0 k\Delta n\ell + j\frac{3}{4\pi}\vec{J}_0 \cdot \frac{\vec{k}}{k} k\Delta n\ell, \tag{31}$$

where the modulated terms originate from Eqs. (29) and (30).

The increment of power modulated into the diffusive wave at f_{us} can be given in terms of the probe power using the geometry illustrated in Fig. 2. We recall the definition of radiance is given as

$$\delta^4 P = L\delta^2 A\delta^2\hat{\Omega}, \tag{32}$$

where P is the power.[29] The incremental power added to the modulated diffusive wave over an infinitesimal volume of the US beam (Fig. 2) is given by

$$\delta^5 P_{ac} = L_0 \delta M\delta^2\hat{\Omega}\delta^2 A = L_0 k\Delta n\delta\ell\delta^2\hat{\Omega}\delta^2 A, \tag{33}$$

where $\delta M = k\Delta n \cdot \delta\ell$ and $\delta^2 A\delta\ell$ is the infinitesimal volume of the US beam discussed earlier. The incremental power can be related to the scalar source for the diffusive wave by integrating Eq. (33) over area, or

$$Q_0^{ac} = \iint L_0 \Delta n k\delta^2\hat{\Omega}. \tag{34}$$

Integrating the radiance over all solid angles and employing the definition of the fluence rate [Eq. (1)] allows us to relate the incremental power to the probe fluence rate, or
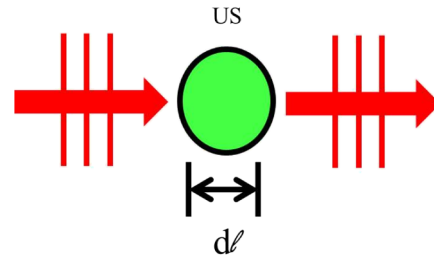
Fig. 2 Geometry. An incident field E_o is modulated by an infinitesimally small ultrasound (US) beam with a width $d\ell$ and produces the field $E_o + ME_o e^{j\omega_{\mathrm{us}}t} + M^*E_o e^{-j\omega_{\mathrm{us}}t}$.

$$Q_0^{ac} = j\frac{2}{\eta}\Phi_0 \Delta nk. \tag{35}$$

Similarly, the dipole source may be written as

$$\vec{Q}_1^{ac} = j\frac{2}{\eta}\vec{J}_0 \Delta nk. \tag{36}$$

We see the monopole source depends on the probe fluence rate and the dipole depends on the flux.

4.1 Single Source

Typically, the monopole and dipole source terms are combined to create an equivalent point source. This is because the photon fluence rate appears to originate from a single, isotropic source at distances $> \ell_t'$.[22,24,30] To apply the same approximation to the modulated light, we need to find the position of this equivalent source. To accomplish this, we will solve for the US-modulated fluence rate using the linear superposition of the dipole and monopole source, or

$$\Phi_{ac}(\vec{r},t) = \frac{A_m}{\vec{r}} - \frac{A_D}{4\pi(\vec{r}+d/2)} + \frac{A_D}{4\pi(\vec{r}-d/2)}, \tag{37}$$

where A_m is the amplitude of the monopole source. The dipole source is represented by two oppositely charged monopoles that have equal amplitudes, A_D, and are separated by a distance h. The monopole amplitude is given by the volume integral

$$A_m = \iiint_V Q_0^{ac} dV. \tag{38}$$

The reader is reminded that A_m is a sum of the total incremental power in the positive sideband described in Eq. (33). Similarly, the dipole–distance product is given by

$$hA_D = \ell_t' \iiint_V \vec{Q}_1^{ac} \cdot \hat{n}\, dV, \tag{39}$$

where $\hat{n}$ is the normal and the volume integral measures the divergence of $\vec{Q}_1(\vec{r},t)$. Using the far-field approximation, we can expand the dipole fractions using the Maclaurin series. After the necessary approximations, we find

$$\Phi_{ac}(\vec{r},t) \approx \frac{A_m}{4\pi(\vec{r}-hA_D/A_m)}. \tag{40}$$

It is interesting to note the amplitude of the equivalent isotropic source relies only on the monopole term. This is expected as the positive and negative point sources will negate each other at distances far from the dipole and, therefore, will only affect the apparent position of the monopole if it is not centered between the sources. The position of the source is given by an offset from the US dot:

$$\vec{\Delta} = \frac{\vec{Q}_1^{ac}}{Q_0^{ac}}h = \frac{\vec{J}_0}{\Phi_0}\ell_t', \tag{41}$$

where Eqs. (38) and (39) were utilized to find the monopole strength and dipole–distance product, respectively.

The derivation of the source strength and offset above assumes the effect of the US–optical interaction may be modeled by a phase shift in the optical field. However, at low US frequencies, the US-induced harmonic motion of scatters may not be ignored. Sakadžić and Wang[12] developed autocorrelation functions for the signal due to change in index of refraction, motion of scatterers, and their cross-correlation. The ratio of coefficients from their work may be utilized to determine the monopole source from our calculation. However, the calculation of the dipole source, and thus the location of the effective source, would require repetition of the present work with consideration of particle motion.

5 Modulated Diffusion Equation

We will use the Green's function derived in the previous sections to create a diffusion equation for a modulated diffusive wave in a semi-infinite, homogeneous turbid medium. We have chosen this geometry because it is commonly utilized in biomedical applications. The goal of this section is to relate the probe beam's power, the US strength, and depth to the diffusely reflected, US-modulated signal in a semi-infinite, homogeneous medium. For this discussion, our probe beam is an infinitesimally narrow, monochromatic source, normally incident upon the surface of a scattering medium as illustrated in Fig. 3. The probe source is located at the origin of the coordinate system and the positive z-axis points down into the medium. The medium has homogeneous reduced scattering and absorption coefficients that satisfy $\mu_a \ll \mu_s'$. This geometry has been discussed in detail elsewhere and is well known. We will briefly review the details and the boundary conditions here for completeness.

The light source enters the medium at the origin and is approximated by an equivalent isotropic source located one transport mean-free path (ℓ_t') down in the medium. The US dot is located some distance away from the point source along the optical axis and has a radius, R_{us}. In order to estimate the fluence and flux at the US dot, we stipulate $z_{us} - R_{us} > 2\ell_t'$. Using the diffusion approximation, the fluence rate at an infinitesimally small US dot is given as

$$\tilde{\Phi}_0(z=z_{us}) = \frac{ca'}{4\pi D}\frac{\exp[jk_D(z_{us}-\ell_t')]}{z_{us}-\ell_t'}, \tag{42}$$

where $a' = \mu_s'\ell_t'$ is the scattering albedo. To clarify subsequent discussions, parameters and values pertaining to the diffusion equation will be denoted with a superscript ˜. The effect of the boundary conditions are negligible at the modulation location and may be ignored. The diffusive wave number is given as

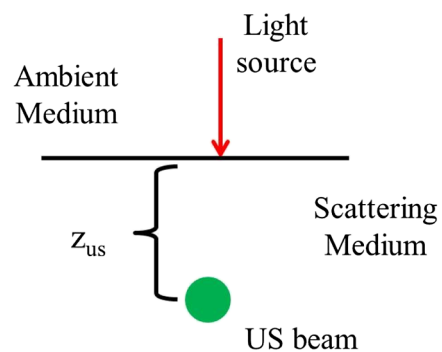$$k_D = \sqrt{(-c\mu_a + j\omega_M)/D}, \tag{43}$$

Fig. 3 Geometry for diffusion model.

where ω_M is the angular modulation frequency. The imaginary part of k is the effective attenuation coefficient. We are assuming the boundary conditions are negligible at the depth z_{us}. The flux may be approximated as

$$\vec{J} = -\frac{D}{c}\nabla\tilde{\Phi}. \tag{44}$$

This approximation is typically valid for frequencies that are <1 GHz.[23]

As mentioned above, the US dot creates a modulated diffusive wave originating from a point. The point is offset from the US dot to account for the probe beam's flux, as stipulated by Eq. (41), with a strength given by Eq. (38). The offset is entirely along the z axis because the US dot is in line with the optical axis. To emphasize this, we will replace $\vec{\Delta}$ with Δz. The equivalent source is shown in Fig. 4(a).

The distance between the equivalent point source and the measurement location with the coordinates x_m, y_m, and $z_m = 0$ is illustrated by r_1 in Fig. 4(b) and given by

$$r_1 = \sqrt{x_m^2 + y_m^2 + (z_{us} + \Delta z)^2}. \tag{45}$$

As mentioned earlier, the extrapolated boundary conditions require an equivalent negative point source at some distance above the surface of the medium. Figure 4 illustrates the negative point sources for both the probe and US-modulated diffusive waves. The negative point source forces the radiance to be zero on a plane with a position along the z axis defined by

$$z_b = -2AD, \tag{46}$$

where A is a constant related to the index of refraction mismatch at the boundary interface.[26,27] The negative sign implies the plane is above the medium. We will assume a matched index of refraction, so that $A = 1$. The distance between this negative, modulated point source and the measurement location is given by
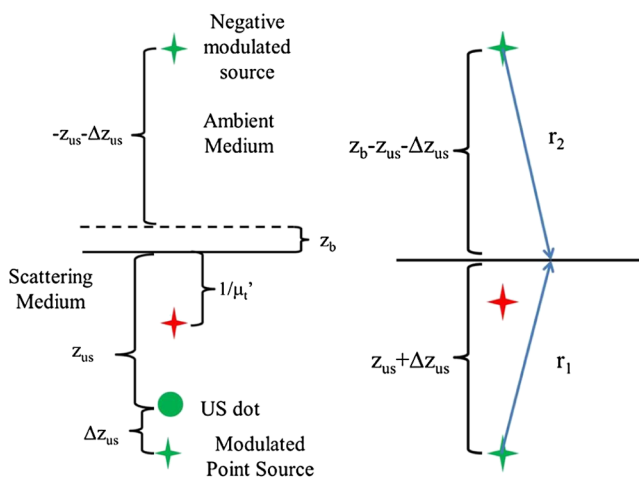
Fig. 4 (a) Geometry for diffusion model. The probe beam is converted to an equivalent source one transport mean-free path deep in the tissue and the US dot is located at z_{us}. The modulated diffusive wave's origin is offset from the US beam, along the z axis, and is given by Δz. The fluence goes to zero at z_b above the medium. (b) The measurement location is located r_1 and r_2 distance away from the positive and negative point sources, respectively.

$$r_2 = \sqrt{x_m^2 + y_m^2 + (-z_{us} - \Delta z + z_b)^2}. \tag{47}$$

Using these terms, we can approximate the diffusely modulated fluence rate at a measurement location on the boundary as a superposition of the two sources, or

$$\tilde{\Phi}_{ac}(x, y, 0) = \frac{cA_m}{4\pi D}\left[\frac{\exp(jk_D r_1)}{r_1} - \frac{\exp(jk_D r_2)}{r_2}\right]$$
$$\times \exp(-j\omega_M t). \tag{48}$$

It is important to note that the boundary conditions must be included and, hence, the need for a negative point source in this case. Assuming a numerical aperture of 1 and that the scattering medium is index matched to the ambient medium, the reflectance at the boundary is[23]

$$\tilde{R}_{ac} = \frac{1}{4}\tilde{\Phi}_{ac} + \frac{1}{2}\nabla\vec{J}_{ac} \cdot \hat{n}, \tag{49}$$

where $\hat{n}$ is the unit vector pointing along the negative z axis. This is typically simplified by assuming the flux vector, and thus the gradient of the fluence, is normal to the boundary so that

$$\nabla\tilde{\Phi} \approx \frac{\delta}{\delta z}\tilde{\Phi} \tag{50}$$

at the boundary.

This section derived a closed-form solution that relates the modulated diffusive wave to an initial probe beam in a semi-infinite homogeneous medium. Calculating the flux at the US beam becomes complicated if the radius of the US dot is on the size order of the probe beam's diffusive wave and must be solved using convolution. Of course, this solution may be utilized in other geometries with the application of appropriate boundary conditions.

6 FDTD Simulation

We will utilize a numerical simulation of US and light interaction to verify the parameters derived in Secs. 3 and 4. The simulation utilizes a two-dimensional FDTD solution to Maxwell's equations to propagate an optical field through a scattering medium. The effect of the US beam is modeled for different phases, and the results are linearly combined to find the modulated field. This model has been described elsewhere,[18,31] so we will discuss only the salient features here.

The FDTD is utilized to propagate a TM_z polarized optical field, where the z axis is the third dimension that is not simulated. To keep units consistent with physical quantities, it is assumed the medium extends 1 m along the third dimension. Maxwell's equations were discretized in time step sizes of 0.89 fs and pixels of 47.4×47.4 nm. The simulation was allowed to run for 20,000 time steps (or ∼1.79 ps) to ensure the optical wave reached steady-state conditions within the simulated medium. We verified the wave reached steady state by examining the time histories. Each simulation took ∼28 h in MATLAB® (R2012a, The MathWorks, Natick, MA) for an area of 130×160 μm^2 along the width and depth dimensions, respectively, running on a Platform HPC 3.0 on Red Hat Enterprise Linux 6.1 named Venture at Northeastern University. The cluster has 80 nodes, each with dual-core processors

and between 4 and 8 GB of RAM. The queue system is a load sharing facility engine.
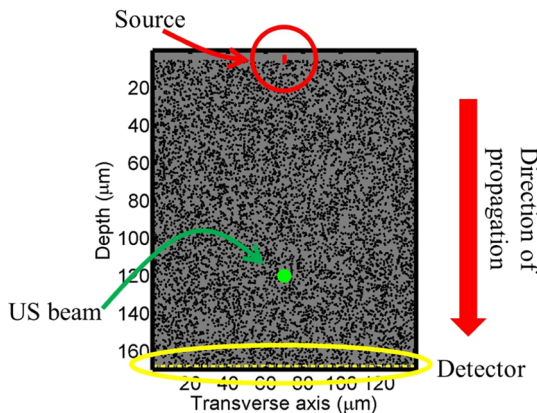
6.1 Synthetic Phantom

A synthetic phantom was created to simulate a highly scattering medium shown in Fig. 5. The phantom simulates titanium oxide ($n = 1.48$) suspended in gel ($n = 1.33$) and is similar to phantoms used in previous scattering experiments[32] and simulations.[18] This is a two-dimensional simulation, so the scatterers are actually cylindrical, and to preserve the units for our numerical calculations, we assume they extend 1 m along the third dimension. The phantom measures 130×155 μm and contains ~9700 randomly distributed cylinders. The cylinders have a diameter of 532 nm but are allowed to overlap so they can make complicated shapes. The high density of scatterers and their irregular shapes indicate that we may not use Mie scattering to characterize this medium.[33] Even though the particles are randomly distributed, their positions are fixed for all simulations. The reduced scattering coefficient was determined by comparing the flux and fluence rate using

$$\mu_s' = -\frac{\nabla \Phi_0}{3\vec{J}_0}. \tag{51}$$

The reduced scattering coefficient is 680 cm^{-1} and $\ell_t' = 14.7$ μm. While the reduced scattering coefficient is over an order of magnitude larger than expected for most tissue, it was chosen so that diffusion effects may be observed within a reasonable computational area. This phantom does not contain absorbers.

The US modulation is modeled as a cylindrical beam with a diameter of 7.4 μm centered at 120 and 70 μm along depth and transverse axis, respectively, and is illustrated in green in Fig. 5. The diameter is ~25% greater than the US wavelength in tissue. This model would be difficult to implement physically, but it provides insight into the microscale effects of modulation. A plane wave with a wavelength of 632 nm is turned on and plateaus at full intensity after 1.4 fs. The beam extends 1.9 μm along the transverse axis.

Fig. 5 Geometry of the synthetic scattering phantom. The scatterers are randomly distributed throughout the medium and have a radius of 532 nm. The index of refraction of the scatterers is 1.48, and they are embedded in a medium with $n = 1.33$. The US dot is illustrated in green and is centered at 60 and 65 μm along the depth and transverse dimensions, respectively. The US dot has a radius of 7.4 μm.

7 Results

As discussed above, a probe beam is utilized to interrogate the scattering medium described in Sec. 6.1. The resulting irradiance, as simulated by the FDTD model, is illustrated in Fig. 6(a), where the scattering medium is illustrated in gray and the probe's irradiance is illustrated in red. The probe's Poynting vector distribution is illustrated in Fig. 6(b). The direction of the Poynting vector is illustrated with color, where red indicates the vector is directed down along the depth axis and cyan indicates a vector in the opposite direction. The intensity of the graph's colors indicates the magnitude of the Poynting vector. Pixels containing a magnitude below a given threshold are set to white.

The fluence rate of the probe beam is found using Eq. (21) and the FDTD-simulated irradiance. The reader is reminded that results derived using the diffusion approximation will be denoted with a superscript $(\tilde{\ })$. The ensemble average is computed by convolving the irradiance with a uniform 5×5 μm mask using MATLAB®'s conv2 function. The mask size was chosen to minimize the appearance of coherent effects, and the resulting fluence rate is illustrated in Fig. 6(c). Similarly, the flux is calculated utilizing Eq. (22) and is illustrated in Fig. 6(d).

It is interesting to note that both the Poynting vector and flux exhibit a strong component in the forward direction as well as two side lobes. These side lobes have a divergence that is predicted by diffraction for a rectangular aperture[29]

$$\theta_{\text{div}} = \frac{2\lambda}{D_\ell n}, \tag{52}$$

where D_ℓ is the width of the incident beam. For our aperture size of 1.9 μm, $\theta_{\text{div}} = 29$ deg. The blue line in Fig. 6(b) diverges from the normal at θ_{div} and predicts the divergence angle of the probe beam, at shallow depths, accurately. It is important to note that the RTE does not predict the existence of these coherent effects.

7.1 Sideband

The US dot is introduced and the probe field is modulated to create sidebands at frequencies $f_{\text{opt}} \pm f_{\text{us}}$. The sidebands are symmetric around the carrier frequency, so that their irradiances have the relationship $I(f + f_{\text{us}}) = I(f - f_{\text{us}})$, though there is a $180 - \text{deg}$ phase shift between the two fields. The fluence rates for both sidebands are illustrated in Fig. 7(a). As discussed in Sec. 4.1, we see the flux from the probe beam is encoded in the sideband and the fluence is not uniformly distributed around the US beam. The sideband's flux is illustrated in Fig. 7(b) and exhibits a strong downward component.

The optical power modulated into the sideband may be computed by using the divergence theorem, which states

$$P_{ac} = \iiint_V \nabla \cdot \vec{S}(\vec{r}) dV, \tag{53}$$

where V is an arbitrary volume that encloses the US beam source. Figure 8 demonstrates the enclosed power in the sideband within a cylinder centered on the US dot for varying radii. The enclosed power increases with cylinder diameter and reaches a steady state just past 3.7 μm, which is the US dot's radius. The total power in the sideband is 0.05 pW. It is
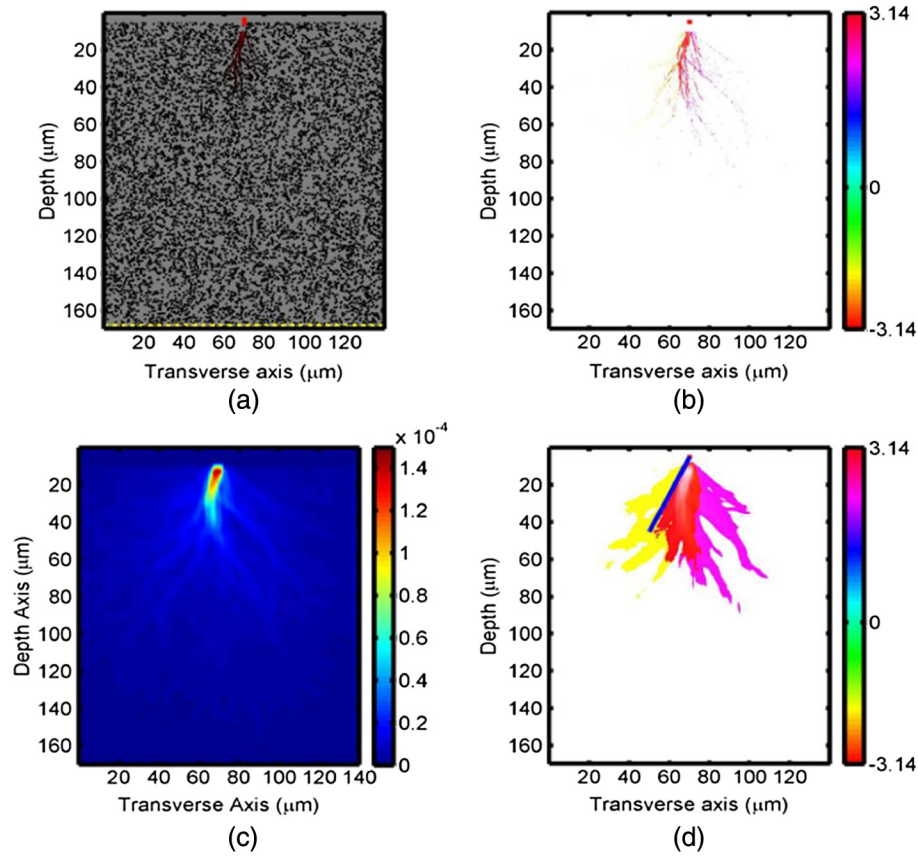
Fig. 6 A collimated beam is propagated through the synthetic medium shown in Fig. 5 utilizing a finite-difference time-domain (FDTD) simulation. (a) A visualization of the resulting irradiance (red) superimposed on the medium (gray). The source's position is illustrated by the solid red line (top of the figure). (b) The magnitude and direction of the calculated Poynting vector in the medium. The intensity of the pixels represents the magnitude of the Poynting vector, with pixels containing a magnitude below a given threshold set to white. The color of the pixels illustrates the direction of the vector with units of radians. The fluence rate (c) is calculated using Eq. (21). The colorbar has units of w/m^2. The flux in (d) is calculated using Eq. (22) and is displayed in a similar manner as the Poynting vector in (b). It is interesting to note that the light diverges within the medium at approximately the divergence angle. The blue line represents the divergence angle of 632 nm light from the light source as calculated by Eq. (52).
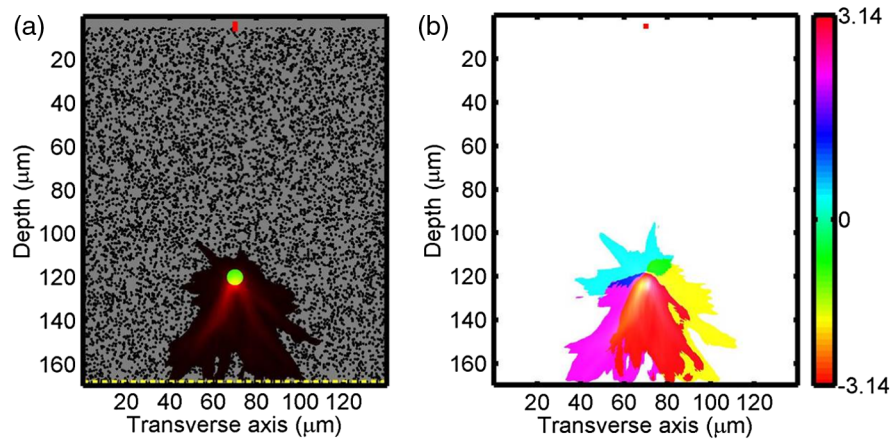
Fig. 7 FDTD results for (a) the US-modulated sideband's fluence rate (red) is illustrated superimposed on the synthetic scattering medium (gray). The US dot's location is illustrated by the solid green circle. (b) The magnitude and direction of the modulated flux is illustrated. As in Fig. 6 figure, the color and intensity of the pixels illustrate the direction and magnitude of the vector, respectively. We see the modulated flux vector continues to be weighted in the depth direction.
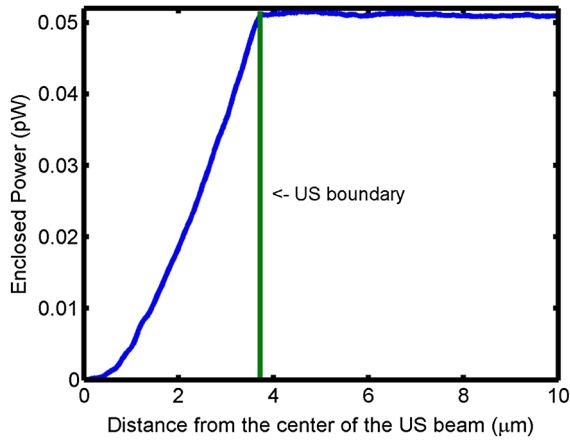
Fig. 8 Power in the sideband, as simulated by the FDTD and computed using divergence theorem in Eq. (53). As expected, the enclosed power increases until it reaches the boundary of the US beam at 3.7 μm and is $\sim$0.05 pW.

interesting to note that the enclosed power would not be a constant if the optical signal did not reach steady state.

We use the power modulated into the diffusive wave to calculate the modulation cross section:

$$\sigma_{\text{calc}} = \frac{P_{ac}}{\Phi_0}. \tag{54}$$

We can compare this to the predicted cross-section, which should be proportional to the surface area of the US dot, or

$$\sigma_p \approx \pi d \cdot z, \tag{55}$$

where d is the diameter of the US dot. The reader is reminded that the unsimulated dimension for the FDTD is assumed to extend for 1 m, so $z = 1$ m. We use the circumference to account for the fact that the US dot is illuminated from all directions. We calculate the cross-section to be $\sigma_{\text{calc}} = 22$ μm^2 using the simulation data and $\sigma_p = 23$ μm^2 using the approximation in Eq. (55).

7.2 Modulated Diffusive Wave

The modulated fluence rate (at f_{us}) may be calculated from the FDTD simulations as follows:

$$\Phi_{ac} = \left\langle \frac{E_0 E_-^* + E_+ E_0^*}{\eta} \right\rangle, \tag{56}$$

where E_0, E_-, and E_+ are the baseband and negative and positive modulated fields, respectively. Figure 9(a) illustrates Φ_{ac}. We see that the effect of the US dot is visible and that Φ_{ac} is at a maximum within its diameter. We also note that Φ_{ac} is small near the surface of the scattering medium even though the probe beam is at a maximum. It is interesting to note the complex signals from the sideband and carrier frequencies are encoded in the result as real numbers and can be negative. This is still physical because the fluence rate for the entire signal is >0.
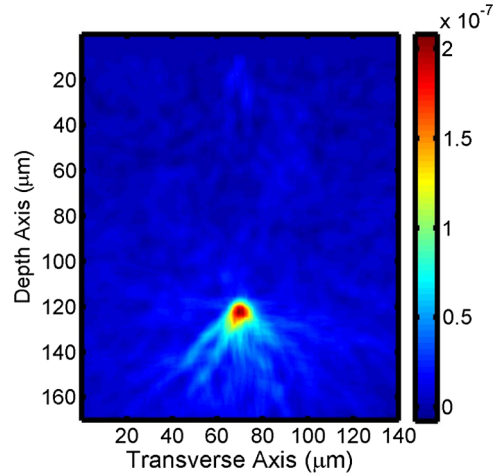
Fig. 9 Fluence rate for the diffusive wave modulated at f_{us}. The color bar represents intensity in W/m^2.

7.2.1 Verifying ac diffusive wave's source location

The single-source diffusion approximation, discussed in Sec. 4.1, suggests that diffusive light appears to be emitted by a single isotropic point source. The location of the isotropic point source for the initial probe beam, for the geometry illustrated in Fig. 5, is one transport mean-free path along the depth axis and in the medium as described in Sec. 2. However, the equivalent isotropic source for the modulated (or ac) diffusive wave must incorporate the flux of the probe beam as described in Sec. 4.1. We can use the simulated probe beam to predict the modulated isotropic source's location using Eq. (41). To account for the finite size of the US beam, the result is averaged over its volume. The predicted offset from the center of the US beam is 6 μm along the depth direction and 1 μm along the x axis. As expected, the offset is primarily along the depth direction.

This source location should be similar to the intensity-weighted center of the actual fluence rate of the modulated diffusive wave (shown in Fig. 9), which is found using

$$\vec{c} = \frac{\iiint_V \Phi_{ac}(\vec{r})\vec{r}\,dv}{\iiint_V \Phi_{ac}(\vec{r})\,dv}, \tag{57}$$

where V is the volume of interest. The center of the actual modulated diffusive wave's fluence rate is offset from the center of the US dot by 7.4 μm in the depth direction and -0.5 μm along the x axis.

Table 1 The resulting modulated power and offset of the equivalent isotropic point source for varying depths of z_{us}.

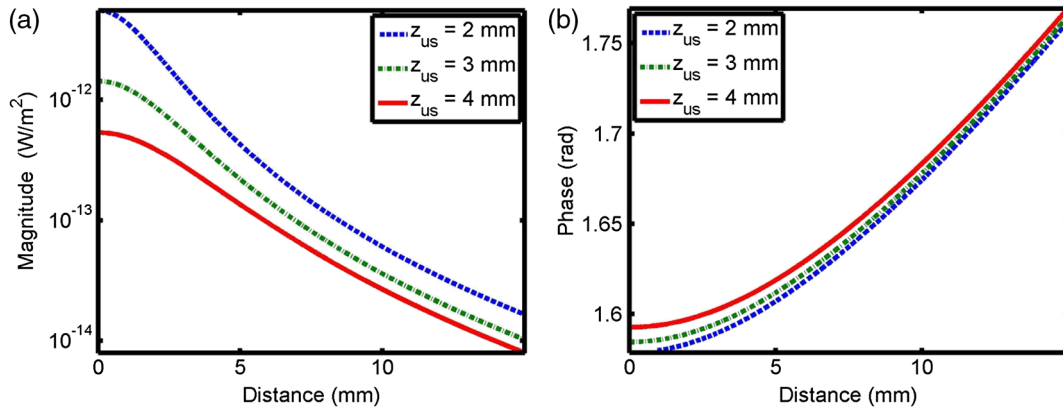| z_{us} (mm)	Modulated power (fW)	Offset (mm)
2	79.1	0.351
3	37.4	0.185
4	23.6	0.129

Fig. 10 The resulting modulated diffusive wave magnitudes (a) and phases (b) for varying US depths.

7.2.2 *Verifying ac diffusive wave's source strength*

Equation (40) illustrates that the strength of the equivalent isotropic source for the ac diffusive wave is given by the monopole term A_m. Using Eq. (38), we can predict the monopole's strength, using the simulated probe beam, and the result is $A_m = 12.7$ pW. This equivalent source strength encompasses all the power in the modulated diffusive wave. We compare the predicted results to the actual power modulated into the positive frequency diffusive wave, which is found by

$$P_{ac} = 2\sqrt{P_0 P_{sb}}, \tag{58}$$

where $P_0 = 6.9$ nW is the initial probe power, and we get the sideband power from Fig. 8, $P_{sb} = 50$ fW. The resulting modulated power in the simulated diffusive wave is 11.7 pW.

8 Diffusion

We will utilize the discussion in Sec. 5 to analyze US-modulated diffuse reflectance from a semi-infinite turbid medium. This medium is illuminated with a normally incident, infinitesimally narrow laser beam with a wavelength of 633 nm as shown in Fig. 3. The turbid medium has homogeneous optical properties with $\mu_s' = 10$ cm^{-1} and $\mu_a = 0.01$ cm^{-1}, which are similar to biological tissue.[24,34]

The initial probe fluence rate is simulated using the steady-state diffusion approximation in Eq. (42). The flux is then calculated using Eq. (44). The resulting diffused light is modulated by a focused, 50-MHz US beam. The beam is modeled as a uniform sphere with 29 μm radius and is located on axis with the optical source. The index of refraction is uniformly modulated within the US sphere by a factor of 1/1000. The resulting diffusive wave can now be modeled by an equivalent isotropic source with strength given by Eq. (38). The source is offset from the center of the US sphere with a distance given by Eq. (41).

Table 1 illustrates the resulting strength of the modulated equivalent isotropic source, and its offset, for increasing depth locations z_{us} of the US sphere. We note that the modulated reflectance is small. This is, in part, due to the relatively small cross-section of the US dot, which is $\sigma_p = 2.6$ nm^2. We note the modulated power decreases exponentially as the US sphere probes greater depths. It is interesting to note the offset also decreases with depth.

The parameters in Table 1 were utilized to solve for the diffuse reflectance using Eq. (49). Figure 10(a) illustrates the resulting reflectance, on a log plot, of the modulated diffusive waves for US dots at varying depths. The geometry is radially symmetric around the optical source, so the results are presented in radial coordinates. As expected, the peak power occurs at $\rho = 0$ and the signal decays exponentially with distance. We also see the slopes of the modulated reflectance curves vary even though the turbid medium is unchanged. This implies the slope of the US modulated diffuse reflectance depends on both the optical properties of the medium and the position of the US modulation. It is interesting to note that the probe beam diffuse reflectance will have a slope related to the effective attenuation coefficient.

9 Conclusion

This paper developed a Green's function for US-modulated diffuse reflectance. We linked the incident optical probe and the US-modulated field, and developed a relationship for the US-modulated radiance. We then applied the P-1 approximation to the RTE to create a diffusion equation for the modulated diffusive wave. We then simulated US modulation of a probe beam using a previously published model and the results were utilized to validate our predicted values. We also used these results to verify the approximate effective cross-section of a US dot in a scattering medium. Although the results were demonstrated on a relatively unrealistic geometry, the equations presented are general enough to be applied elsewhere.

We illustrated the strength of this approach by developing a closed form solution that relates the incident probe power and the US strength and depth to the received optical signal. Finally, we demonstrated the effect of varying the US modulation depth on the modulated diffusive wave.

References

1. M. Rajadhyaksha et al., "In vivo confocal scanning laser microscopy of human skin: melanin provides strong contrast," *J. Invest. Dermatol.* **104**, 946–952 (1995).
2. T. W. Murray et al., "Detection of ultrasound-modulated photons in diffuse media using the photorefractive effect," *Opt. Lett.* **29**(21), 2509–2511 (2004).

3. F. J. Blonigen et al., "Computations of the acoustically induced phase shifts of optical paths in acoustophonic imaging with photorefractive-based detection," *Appl. Opt.* **44**(18), 3735–3746 (2005).

4. A. Bratchenia et al., "Acousto-optic-assisted diffuse optical tomography," *Opt. Lett.* **36**(9), 1539–1541 (2011).

5. S. R. Kothapalli and L. V. Wang, "Ultrasound-modulated optical microscopy," *J. Biomed. Opt.* **13**(5), 054046 (2008).

6. X. Xu, H. Liu, and L.V. Wang, "Time-reversed ultrasonically encoded optical focusing into scattering media," *Nat. Photonics* **5**, 154–157 (2011).

7. Y. M. Wang et al., "Deep-tissue focal fluorescence imaging with digitally time-reversed ultrasound-encoded light," *Nat. Commun.* **3**, 928 (2012).

8. B. Judkewitz et al., "Speckle-scale focusing in the diffusive regime with time reversal of variance-encoded light (trove)," *Nat. Photonics* **7**, 300–305 (2013).

9. C. V. Raman and N. S. N. Nath, "The diffraction of light by high frequency sound waves: Part I," *Proc. Indian Acad. Sci.* **3**(5), 406–412 (1936).

10. L. V. Wang, "Mechanisms of ultrasonic modulation of multiply scattered coherent light: an analytic model," *Phys. Rev. Lett.* **87**(4), 043903 (2001).

11. L. V. Wang, "Mechanisms of ultrasonic modulation of multiply scattered coherent light: a Monte Carlo model," *Opt. Lett.* **26**(15), 1191–1193 (2001).

12. S. Sakadžić and L. V. Wang, "Modulation of multiply scattered coherent light by ultrasonic pulses: an analytical model," *Phys. Rev. E Stat. Nonlin. Soft Matter Phys.* **72**(3), 036620 (2005).

13. S. Sakadžić and L. V. Wang, "Correlation transfer equation for ultrasound-modulated multiply scattered light," *Phys. Rev. E* **74**(3), 036618 (2006).

14. S. G. Resink, A. C. Boccara, and W. Steenbergen, "State-of-the art of acousto-optic sensing and imaging of turbid media," *J. Biomed. Opt.* **17**(4), 040901 (2012).

15. Q. Liu, S. Norton, and T. Vo-Dinh, "Modeling of nonphase mechanisms in ultrasonic modulation of light propagation," *Appl. Opt.* **47**(20), 3619–3630 (2008).

16. C. U. Devi, A. K. Sood, and R. M. Vasu, "Application of ultrasound-tagged photons for measurement of amplitude of vibration of tissue caused by ultrasound: theory, simulation, and experiments," *J. Biomed. Opt.* **11**(3), 034019 (2006).

17. G. Bal and J. C. Schotland, "Inverse scattering and acousto-optic imaging," *Phys. Rev. Lett.* **104**(4), 043902 (2010).

18. J. L. Hollmann et al., "Analysis and modeling of an ultrasound-modulated guide star to increase the depth of focusing in a turbid medium," *J. Biomed. Opt.* **18**(2), 025004 (2013).

19. S. Powell and T. S. Leung, "Highly parallel Monte-Carlo simulations of the acousto-optic effect in heterogeneous turbid media," *J. Biomed. Opt.* **17**(4), 045002 (2012).

20. T. S. Leung and S. Powell, "Fast Monte Carlo simulations of ultrasound-modulated light using a graphics processing unit," *J. Biomed. Opt.* **15**(5), 055007 (2010).

21. A. Ishimaru, *Wave Propagation and Scattering in Random Media*, Vol. 2, Academic Press, New York (1978).

22. D. A. Boas, "Diffuse photon probes of structural and dynamical properties of turbid media: theory and biomedical applications," PhD Thesis, University of Pennsylvania (1996).

23. R. C. Haskell et al., "Boundary conditions for the diffusion equation in radiative transfer," *J. Opt. Soc. Am. A* **11**(10), 2727–2741 (1994).

24. L. V. Wang and H. Wu, *Biomedical Optics: Principles and Imaging*, Wiley-Interscience, Hoboken, New Jersey (2007).

25. T. J. Farrell, M. S. Patterson, and B. Wilson, "A diffusion theory model of spatially resolved, steady-state diffuse reflectance for the noninvasive determination of tissue optical properties in vivo," *Med. Phys.* **19**(4), 879–888 (1992).

26. S. E. Orchard, "Reflection and transmission of light by diffusing suspensions," *J. Opt. Soc. Am.* **59**(12), 1584–1597 (1969).

27. J. L. Hollmann, "Multi-layer diffusion approximation for photon transport in biological tissue," Master's Thesis, Texas A&M University. Available electronically from http://hdl.handle.net/1969.1/ETD-TAMU-1901 (2008).

28. L. Wang, S. L. Jacques, and L. Zheng, "MCML–Monte Carlo modeling of light transport in multi-layered tissues," *Comput. Methods Programs Biomed.* **47**(2), 131–146 (1995).

29. C. A. DiMarzio, *Optics for Engineers*, CRC Press, Boca Raton, Florida (2011).

30. J. L. Hollmann and L. V. Wang, "Multiple-source optical diffusion approximation for a multilayer scattering medium," *Appl. Opt.* **46**(23), 6004–6009 (2007).

31. J. L. Hollmann and C. A. DiMarzio, "Modeling optical phase conjugation of ultrasonically encoded signal utilizing finite-difference time-domain simulations," *Proc. SPIE* **8227**, 82270I (2012).

32. I. M. Vellekoop and A. P. Mosk, "Focusing coherent light through opaque strongly scattering media," *Opt. Lett.* **32**(16), 2309–2311 (2007).

33. H. J. Van Staveren et al., "Light scattering in intralipid-10% in the wavelength range of 400–1100 nm," *Appl. Opt.* **30**(31), 4507–4514 (1991).

34. S. T. Flock et al., "Optical properties of intralipid: a phantom medium for light propagation studies," *Lasers Surg. Med.* **12**(5), 510–519 (1992).

Biographies of the authors are not available.